

Quantifying Interparticle Forces and Heterogeneity in 3D Granular Materials

R. C. Hurley,^{1,*} S. A. Hall,^{2,†} J. E. Andrade,¹ and J. Wright³

¹*Division of Engineering and Applied Science, California Institute of Technology, Pasadena, California 91125, USA*

²*Division of Solid Mechanics, Lund University, Lund 22100, Sweden*

³*European Synchrotron Radiation Facility, Grenoble 38000, France*

(Received 11 March 2016; published 24 August 2016)

Interparticle forces in granular materials are intimately linked to mechanical properties and are known to self-organize into heterogeneous structures, or force chains, under external load. Despite progress in understanding the statistics and spatial distribution of interparticle forces in recent decades, a systematic method for measuring forces in opaque, three-dimensional (3D), frictional, stiff granular media has yet to emerge. In this Letter, we present results from an experiment that combines 3D x-ray diffraction, x-ray tomography, and a numerical force inference technique to quantify interparticle forces and their heterogeneity in an assembly of quartz grains undergoing a one-dimensional compression cycle. Forces exhibit an exponential decay above the mean and partition into strong and weak networks. We find a surprising inverse relationship between macroscopic load and the heterogeneity of interparticle forces, despite the clear emergence of two force chains that span the system.

DOI: 10.1103/PhysRevLett.117.098005

Numerous studies have examined the heterogeneity, anisotropy, and statistics of interparticle forces in granular materials. Interparticle forces are known to self-organize into structures called force chains [1], exhibit a roughly exponential decay above their mean [1], and demonstrate complex spatiotemporal fluctuations under external load [2,3]. Understanding these phenomena is crucial for an accurate multiscale picture of granular media from which accurate models can be built.

Discrete element modeling has permitted in-depth study of interparticle forces in granular media composed of spherical and aspherical frictional particles. Experiments to extract interparticle forces—required for validating, augmenting, and calibrating simulations—have been restricted to idealized particles. For instance, a large number of experiments have examined force transmission through two-dimensional (2D) photoelastic [1–3] and rubber disks [4]. Recent work has employed x-ray microtomography and refractive index tomography to study interparticle forces in frictionless three-dimensional (3D) hydrogels and rubber spheres [5,6]. While more realistic, stiff sand grains have been examined in experiments, studies have been limited to quantifying grain strains [7–9], mapping *in situ* 3D grain motion [10], and examining rapid communication during compaction [11]. No experiments have yet inferred forces in 3D, frictional, stiff granular materials like the sands and grains found throughout nature and industry. Such stiff materials may behave differently than the compliant materials studied previously [5,6].

Here, we present experimental results providing the first known measurements of interparticle forces in a 3D, frictional, stiff granular material. We leverage recent advances in 3D x-ray diffraction (3DXRD) and tomography [9,12] to

measure the *in situ* evolution of tensor grain strains as well as the 3D structure of 77 quartz grains during a confined uniaxial compression cycle. We solve an inverse problem [4,13,14] to determine interparticle force vectors that best match these measurements. The statistics and heterogeneity of the resulting forces are compared with past work and a surprising inverse relationship is found between force heterogeneity and macroscopic load.

Experiment.—The granular medium studied was composed of 77 nearly spherical single-crystal quartz grains with diameters ranging from 220 to 310 μm [Fig. 1(b)]. The grains formed a sample 1.5 mm tall by 1.5 mm diameter that was placed in a uniaxial loading device in beam line ID11 at the European Synchrotron Radiation Facility (ESRF), as shown in Fig. 1(a). The sample was loaded with an upward-acting piston while displacement and load were measured with a displacement transducer and top-mounted load cell. At load increments of approximately 5 N, strain was held constant for 70 minutes while 3DXRD and tomography scans were made. Scans were performed with the sample fully illuminated by a monochromatic beam of energy 41.9 keV. Force relaxation on the order of 2–4 N occurred quickly after the loading was stopped for each scan and was quickly recovered upon reloading. An x-ray detector obtained 2D diffraction patterns [Fig. 1(c)] from the sample as it was rotated 180° in increments of 0.25°. Another detector obtained 2D transmission data for tomographic reconstruction as the sample was rotated 180° in increments of 0.1°.

Data analysis: diffraction.—Unit cell parameters were determined for each quartz grain at each load step by indexing, tracking, and fitting diffraction spots [12]. Reference unit cell parameters were determined from the

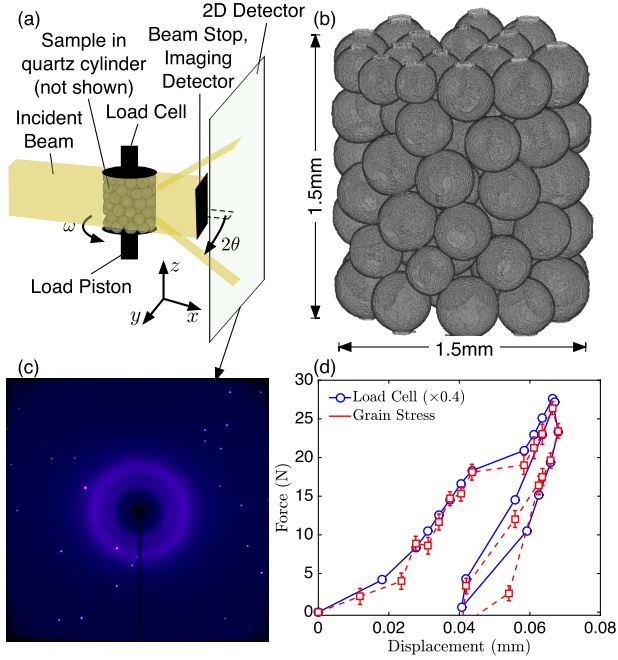


FIG. 1. Experiment setup. (a) Configuration of the specimen and equipment. (b) 3D image of segmented sample reconstructed from x-ray data. (c) Example diffraction pattern from a single acquisition. (d) Macroscopic load measured by the load cell and volume-averaged grain stresses, described in the text.

initial unloaded diffraction measurements. Average strain tensors for each grain, ϵ_α , were computed at each load step by comparing unit cell parameters to their reference values [9,12]. Resulting strain tensors have a per-grain resolution on the order of 10^{-4} [12]. Average grain stress tensors, σ_α , were calculated using the nominal anisotropic elastic constants of cultured monocrystal α quartz [15]. The stress tensors were rotated to the sample coordinate frame and sample stress was calculated using $\sigma_T = (1/V_T) \sum_{\alpha=1}^{77} V_\alpha \sigma_\alpha$, where V_T is the total volume in the quartz cylinder and V_α is the volume occupied by each grain, obtained from the reconstructed tomographic images (see below). The vertical component of the total stress was multiplied by the area of the loading piston to obtain the dashed curve in Fig. 1(d). To compute the error bars, we calculated σ_T 50 times for each load step. In each computation, strain tensor components for each grain were given an artificial error of $\eta 10^{-4}$, where η is a different constant drawn from a standard normal distribution. Error bars represent the standard deviation of these 50 calculations. Because of friction between the load piston and quartz cylinder, load values from the load cell exceed those inferred from the diffraction data. Load cell values presented in Fig. 1(d) are therefore multiplied by 0.4 for a convenient comparison to the trends observed in the diffraction data. Agreement in trend between load cell and grain stress calculations is remarkable and confirms the overall accuracy of our strain measurements.

Data analysis: tomography.—3D tomographic images were reconstructed for each load step from x-ray transmission data using the ASTRA toolbox [16]. The 3D images have a resolution of $(1.4 \mu\text{m})^3$ per voxel. Algorithms including binarization and topological watershed were used in Matlab® to segment the grains from the images and determine grain volumes, grain centroids, and all contact locations and orientations. Contact candidates were identified in the segmented images as those voxels whose immediate neighbors contained two distinct grain or boundary IDs. A minimum of 10 voxels was required for a contact candidate to be considered a true contact. However, the choice of this threshold had little effect on the force inference results described below.

Because of the compliance of the loading system, displacements reported by the displacement transducer consistently exceed those computed from tomographic images. These images were therefore used to obtain true sample displacements in Fig. 1(d).

Data analysis: force inference.—Interparticle forces were obtained using the multiobjective optimization algorithm discussed in [14] with an assumed grain-grain and grain-boundary friction coefficient of 0.7, consistent with experiments [17]. In particular, we found force vectors at all contacts in the system that minimize the sum of two objective functions: one objective function containing equilibrium equations for each grain α and another containing a relationship between forces and the average stress tensor, σ_α , for each grain obtained from 3DXRD. We also used constraints in the optimization algorithm to enforce noncohesive forces and Coulomb friction at each contact. See Supplemental Material [18] and Refs. [4,14] for details on these objective functions and the optimization procedure. The multiobjective optimization problem was solved in Matlab® using the cvx toolbox [19]. The force inference puts no restriction on grain shapes and makes no assumption of contact law.

Contacts and stiffness.—Figure 2(b) shows the total number of contacts, including grain-grain and grain-boundary contacts, extracted from the reconstructed tomographic images at each load step. Figure 2(c) shows the macroscopic stiffness of the assembly obtained by taking the numerical derivative of the load cell data. Stiffness was not computed for steps 11, 16, and 21 due to device issues. Both the number of contacts and the macroscopic stiffness increase during loading until step 10. The number of contacts then decreases until shortly after the peak load while the macroscopic stiffness plateaus and finally reaches a maximum over the same interval. During unloading, the number of contacts decreases slightly before increasing again during reloading. It is interesting, but unknown why, the load steps corresponding to maximum and minimum contact number are offset from those corresponding to maximum and minimum load. This result is fairly insensitive to the voxel threshold used to identify contacts and may be closely related to the particular contact network of the sample. Macroscopic stiffness follows an expected trend,

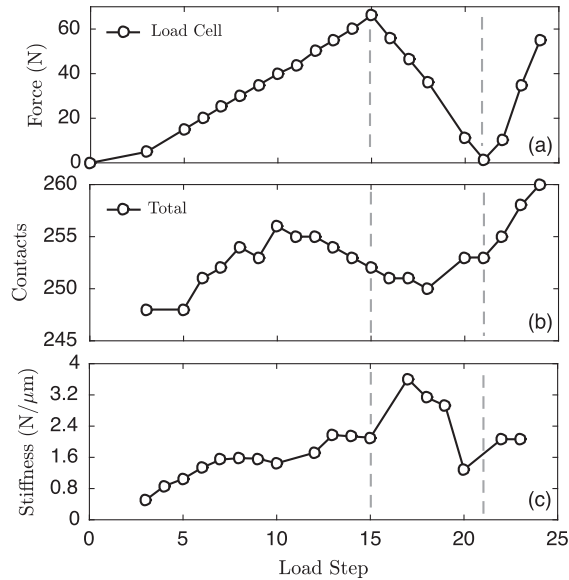


FIG. 2. Evolution of system responses with load step. (a) Macroscopic force from the load cell. (b) Number of total contacts in the system. (c) Stiffness from load cell data. Values at steps 11, 16, and 21 were not computed due to device issues.

reaching a maximum after the peak load, decreasing during unloading, and increasing again during reloading.

Interparticle force evolution.—Interparticle force vectors obtained from the force inference are plotted on the grains at six load steps in Fig. 3(a) [20]. Lines representing force vector magnitudes and directions are centered at contact points. These lines are scaled in length, width, and opacity

by the ratio of force magnitude to the maximum force magnitude in all load steps. Grain surfaces are colored with strain ellipsoids [9]. Grain opacity is scaled by the ratio of grain vertical strain, ϵ_{zz} , to the maximum vertical strain of all grains in all load steps.

Macroscopic loads at the top and bottom boundaries, obtained through force inference, are shown in Fig. 3(c). Forces obtained from the force inference consistently underpredict unscaled values from the load cell and slightly overpredict the σ_T stresses determined by volume averaging of the grain stresses. Since the force inference uses only grain locations, strains, and inferred contact vectors [14], the source of the difference between the force inference and diffraction data is likely a systematic bias in contact location or strain measurement. The agreement in trend of all data sets in Fig. 3(b) is, nevertheless, remarkable and suggests accurate forces, possibly scaled by a measurement bias.

The evolution of interparticle forces in Fig. 3(a) indicates the emergence of two force chains in the system as the load is increased. These force chains are isolated in Fig. 3(b) by plotting only those contact forces, and corresponding grains, carrying at least twice the mean normal force magnitude of the corresponding load step. One force chain spans the system laterally and is evident in all load steps, including during unloading, suggesting force “arching” possibly produced during initial sample preparation. Another force chain, more prominent at high loads, spans the system from the top boundary to the bottom boundary in the front left. Interestingly, the force chains evolve as a function of macroscopic load and are seen to engage different particles before and after unloading.

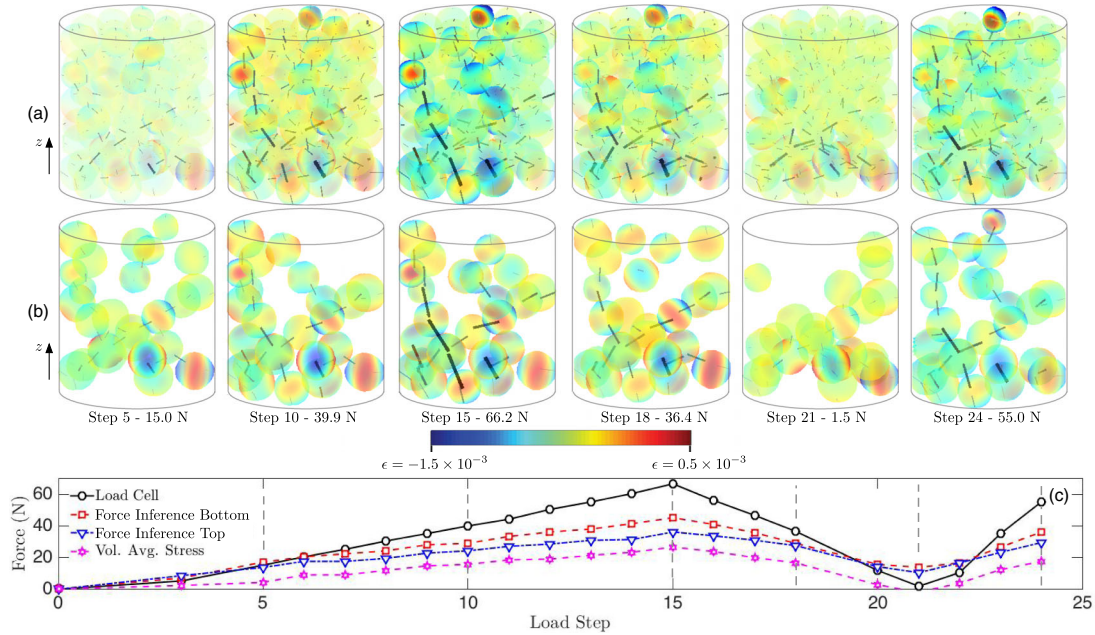


FIG. 3. (a) Force inference results at six load steps on a translucent rendering of grains colored by strain ellipsoids. (b) Force chains found by plotting only forces whose normal magnitude exceeds twice the mean. Corresponding grains are also plotted with 30% opacity. Floating grains occur where force chains diverge. (c) Comparison of vertical forces from various sources.

We further quantify vertical force chain evolution by computing the average spatial autocorrelation coefficient of normal force magnitudes, similar to [1]. In particular, we compute

$$R(r) = \left\langle \frac{\sum_j [f_n^{(i)} - f_n][f_n^{(j)} - f_n]}{\sqrt{\sum_i [f_n^{(i)} - f_n]^2 \sum_j [f_n^{(j)} - f_n]^2}} \right\rangle, \quad (1)$$

where $r = |\mathbf{x}^{(i)} - \mathbf{x}^{(j)}|_2$ is the distance between contacts i and j , $f_n^{(i)}$ is the normal force magnitude at contact i , f_n is the mean normal force magnitude in the system for that load step, and $\langle \dots \rangle$ indicates an average over all contacts i . For this analysis of vertical force chains, both contacts i and j are restricted to those meeting the condition that contact normals, $\mathbf{e}^{(i)}$, are oriented vertically, contact pairs fall within a 30° vertical cone from one another, and contacts pairs are within a distance r from one another. This condition is illustrated in the inset to Fig. 4(a). $R(r)$ shows minimal decrease with increasing r , less than in [1] due to system size. We therefore compute $\langle R(r) \rangle_r$, where $\langle \dots \rangle_r$ indicates an average for all r , and plot the standard deviation as error bars. Results shown in Fig. 4(a) illustrate that correlation between vertically oriented forces increases with macroscopic load. This trend mirrors the visual prominence of the vertical force chain in Fig. 3(a), and can be interpreted as a quantitative signature of the vertical force chain evolution. It is interesting to note that correlation reaches a maximum at the same load step as macroscopic stiffness, indicating that force chain evolution may play a role in determining system stiffness. Correlation coefficients computed for horizontal directions show almost no trend with macroscopic load.

Interparticle force heterogeneity.—We observe normal force magnitudes f_n above the mean to follow an exponential distribution, in agreement with past work [1]. The distribution was constructed for each load step by binning forces greater than the mean and dividing by the total number of forces. Because of the small system size, a least-squares fit of the form $p(f_n) \propto e^{\alpha f_n / \langle f_n \rangle}$ has different slopes α depending upon the bin width. Forces are, therefore, fitted to this distribution with bins ranging from $0.15 \langle f_n \rangle$ to $0.75 \langle f_n \rangle$ in increments of $0.01 \langle f_n \rangle$. The nominal values in Fig. 4(b) are the means of α for all distributions and the error bars represent the standard deviation. We did not fit a cumulative distribution to avoid overfitting forces clustered close to the mean.

Remarkably, Fig. 4(b) suggests that force heterogeneity in the system decreases with increasing macroscopic load, even as force chains become more readily evident in Figs. 3(a), 3(b), and 4(a). More negative α implies a higher proportion of forces clustered close to the mean rather than spreading toward higher values. Figure 4(c) corroborates this result in a novel way, by examining the Gini coefficient for normal force magnitudes. The Gini coefficient, often used to represent a nation's income inequality,

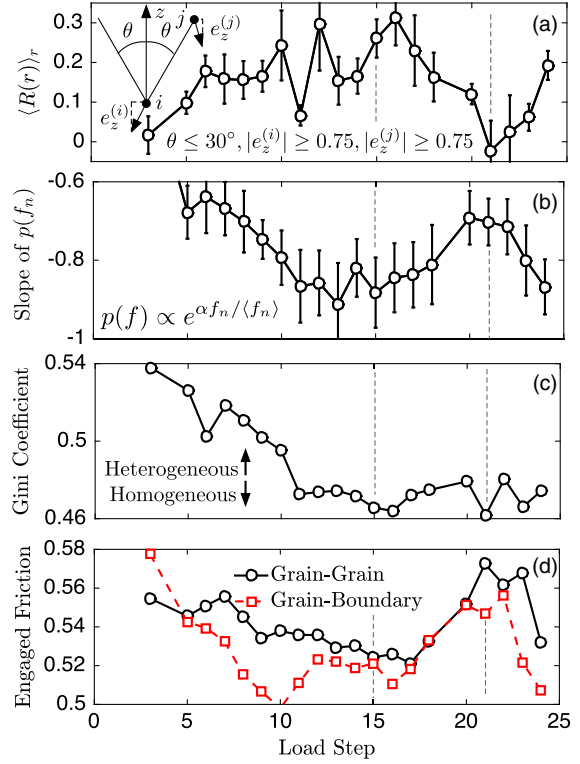


FIG. 4. (a) Average spatial autocorrelation coefficient $\langle R(r) \rangle_r$ for forces aligned vertically as illustrated in the inset. (b) Slope of fit to exponential decay of normal force magnitudes. (c) Gini coefficient computed using all normal force magnitudes in the system. (d) Engaged friction coefficient for grain-grain contacts and grain-boundary contacts. Dashed lines correspond to maximum and minimum loads.

describes the homogeneity of some quantity in a population. A Gini coefficient of unity indicates complete inequality; a value of 0 indicates perfect equality and homogeneity. To calculate the Gini coefficient, we write the normal force magnitudes at all contacts in the vector \mathbf{f}^n in nondecreasing order ($f_i^n \leq f_{i+1}^n$) and compute

$$G = \frac{1}{N_c} \left\{ N_c + 1 - 2 \left[\frac{\sum_{i=1}^{N_c} (N_c + 1 - i) f_i^n}{\sum_{i=1}^{N_c} f_i^n} \right] \right\}, \quad (2)$$

where N_c is the number of contacts. The systematic decrease of the Gini coefficient with load suggests that the forces become more homogeneous with macroscopic load. Similar trends can be observed in data from [9]. Heterogeneity increases with unloading in Fig. 4(b) and to a lesser extent in 4(c); however, homogeneity continues increasing upon reloading. These findings suggest that despite the emergence of force chains and their interpretation as representing increased heterogeneity [1], some aspect of the granular medium's force response actually becomes more homogeneous with load. The different behaviors of α and the Gini coefficient during unloading

suggest that these separate metrics may be sensitive to different characteristics of the force network.

Contact friction and the weak-strong network.—A salient feature of the method described in this Letter, compared to others (e.g., [5,6]), is the ability to infer force vectors at frictional contacts in 3D granular materials. Average “engaged” friction at grain-grain and grain-boundary contacts, computed by averaging the ratio of shear to normal force magnitudes at each contact point, is shown in Fig. 4(d). We observe interparticle friction to be very large in the present system, attaining a minimum value close to 0.52 around load step 16, slightly after the peak load and coincident with peak stiffness. Engaged friction increases to maximum values near 0.58 at low load. The large values of engaged friction are likely a consequence of the system size: the small system prevents particles from moving past one another, increasing friction that may otherwise be relieved by motion.

The inferred interparticle forces demonstrate a division into strong and weak networks in proportions agreeing with past work [21], with approximately 38% of force magnitudes falling above the mean and 62% falling below the mean at all load steps. This so-called bimodal character of forces has not yet been measured in such a small system, providing new experimental evidence of a phenomenon frequently studied numerically.

Conclusion.—This Letter presents the first known experiment allowing *in situ* interparticle force inference in opaque, 3D, frictional, stiff granular materials. This work is made possible by recent advances in 3DXRD, x-ray tomography, and quantitative force inference techniques. Future experiments employing these techniques may be able to provide similar data using 10^3 or more grains. A surprising inverse relationship between force heterogeneity and macroscopic load is observed from this experiment, despite the clear emergence of system-spanning force chains. Spatial autocorrelation of forces across load steps also suggests that the strongest force chains emerge at peak stiffness, during sample unloading. These findings suggest that the present understanding of force chains and their role in the mechanical properties of granular media remains incomplete. Furthermore, these findings imply that widely used metrics such as probability distributions, autocorrelation coefficients, and strong-weak divisions do not capture all of the important characteristics of the force network. Further experiments employing quantitative force inference in 3D, frictional, stiff granular media are needed to further explore force chain behavior. We expect that the present techniques may also aid in calibrating numerical models of complex particle-scale processes such as force chain buckling and grain fracture.

The authors acknowledge the ESRF for synchrotron beam time for proposal ma1913. R. C. H. and J. E. A. acknowledge support from the U.S. Air Force Office of Scientific Research Grant No. FA9550-12-1-0091 and the

U.S. Defense Threat Reduction Agency Grant No. HDTRA1-12-1-0041. S. A. H. acknowledges support from a Marie Curie FP7 integration grant within the 7th European Union Framework Programme. Part of this work was performed under the auspices of the U.S. Department of Energy by Lawrence Livermore National Laboratory under Award No. DE-AC52-07NA27344.

*Present address: Lawrence Livermore National Laboratory, Livermore, CA 94550, USA.

†Corresponding author.
stephen.hall@solid.lth.se

- [1] T. S. Majmudar and R. P. Behringer, *Nature (London)* **435**, 1079 (2005).
- [2] D. Howell, R. P. Behringer, and C. Veje, *Phys. Rev. Lett.* **82**, 5241 (1999).
- [3] A. H. Clark, L. Kondic, and R. P. Behringer, *Phys. Rev. Lett.* **109**, 238302 (2012).
- [4] R. Hurley, E. Marteau, G. Ravichandran, and J. E. Andrade, *J. Mech. Phys. Solids* **63**, 154 (2014).
- [5] N. Brodu, J. A. Dijksman, and R. P. Behringer, *Nat. Commun.* **6**, 6361 (2015).
- [6] M. Saadatfar, A. P. Sheppard, T. J. Senden, and A. J. Kabla, *J. Mech. Phys. Solids* **60**, 55 (2012).
- [7] S. A. Hall, J. Wright, T. Pirling, E. Andò, D. J. Hughes, and G. Viggiani, *Granular Matter* **13**, 251 (2011).
- [8] M. B. Cil, K. Alshibli, P. Kenesei, and U. Lienert, *Nucl. Instrum. Methods Phys. Res., Sect. B* **324**, 11 (2014).
- [9] S. A. Hall and J. Wright, *Geotech. Lett.* **5**, 236 (2015).
- [10] E. Andò, S. A. Hall, G. Viggiani, J. Desrues, and P. Bésuelle, *Acta Geotech.* **7**, 1 (2012).
- [11] N. D. Parab, B. Claus, M. C. Hudspeth, J. T. Black, A. Mondal, J. Sun, K. Fezzaa, X. Xiao, S. Luo, and W. Chen, *Int. J. Impact Eng.* **68**, 8 (2014).
- [12] J. Oddershede, S. Schmidt, H. F. Poulsen, H. O. Sørensen, J. Wright, and W. Reimers, *J. Appl. Crystallogr.* **43**, 539 (2010).
- [13] J. E. Andrade and C. F. Avila, *Granular Matter* **14**, 51 (2012).
- [14] R. C. Hurley, K. W. Lim, G. Ravichandran, and J. E. Andrade, *Exp. Mech.* **56**, 217 (2016).
- [15] P. Heyliger, H. Ledbetter, and S. Kim, *J. Acoust. Soc. Am.* **114**, 644 (2003).
- [16] W. J. Palenstijn, K. J. Batenburg, and J. Sijbers, in *13th International Conference on Computational and Mathematical Methods in Science and Engineering, CMMSE (2013)*, Vol. 2013.
- [17] J. Byerlee, *Pure Appl. Geophys.* **116**, 615 (1978).
- [18] See Supplemental Material at <http://link.aps.org/supplemental/10.1103/PhysRevLett.117.098005> for a full description of the optimization equations and procedure.
- [19] M. Grant, S. Boyd, and Y. Ye, CVX: MATLAB software for disciplined convex programming, <http://cvxr.com/cvx>, 2008.
- [20] See Supplemental Material at <http://link.aps.org/supplemental/10.1103/PhysRevLett.117.098005> for a video of each plot in Fig. 3(a) being rotated 360°.
- [21] F. Radjai, D. E. Wolf, M. Jean, and J.-J. Moreau, *Phys. Rev. Lett.* **80**, 61 (1998).